3. Martian Atmosphere and Its Effects on Propagation

3.1 Introduction

When high-frequency radio waves pass through the Martian atmosphere, the signals also experience attenuation and impairment as they do in Earth's atmosphere. The signal degradation mainly takes place in the lower part of the atmosphere: the troposphere. The propagation medium in the Martian troposphere includes gases, water vapor, cloud, fog, ice, dust and aerosols (haze), etc. The impairment mechanisms include absorption, scattering, refraction, diffraction, multipath, scintillation, Doppler shift, etc. Impairment phenomena include fading, attenuation, depolarization, frequency broadening, ray bending, etc. To measure the degradation of the signals, the following observable parameters are usually used: amplitude, phase, polarization, frequency, bandwidth, and angle of arrival. However, compared with Earth's atmosphere, the Martian atmosphere is thin. Thus, we expect a much smaller tropospheric effect on radio wave propagation.

Before we study radio wave propagation in the Martian atmosphere, it is interesting to calculate the speed of sound v_s at the Martian surface

$$v_s = \sqrt{\frac{\gamma P_0}{\rho_0}} \tag{3-1}$$

where γ is adiabatic index of the gases (~1.35), P_0 is surface atmospheric pressure (6.1 mb), and ρ_0 is surface atmospheric mass density (0.02 kg/m^3). Thus, the speed of sound at Mars is 206 m/s, while the speed at Earth is 331 m/s. Actually, the Martian atmosphere is so much thinner that it is hard for a sound wave to propagate. Consequently, it will be necessary for future Martian colonists to use radio wave communications.

Most Martian tropospheric parameters are those studied in Martian meteorology, such as its pressure, temperature, and wind. Based on measurements from the Vikings and from Mars 6, a nominal mean model for pressure and temperature was obtained [Seiff, 1982]. Table 3-1 lists temperature, pressure, and atmospheric mass density as a function of altitude with 2-km increments for a daily summer-seasonal mean mid-latitude atmosphere. Table 3-1 also gives the ratio p/p_0, as well as pressure values, so that the model may be applied to other values of p_0 than those selected for other times in the summer seasons. The model has the following equation form:

$$\frac{p}{p_0} = \exp\left[-\frac{\mu}{R} \int_{z_0}^{z} \frac{g(z)}{T(z)} dz \right] \tag{3-2}$$

Table 3-1. Nominal Summer-Seasonal Mid-Latitude Martian Atmospheric Model

			Northern Summer			Southern Summer	
z, km	T, K	p/p_0	p, mb p_0 = 6.36	ρ, kg/m^3	g, m/s^2	p, mb p_0 = 7.3	ρ, kg/m^3
0	214	1.000	6.36	1.56×10^{-2}	3.730	7.30	1.78×10^{-2}
2	213.8	0.833	5.30	1.30	3.725	6.08	1.49
4	213.4	0.694	4.41	1.08	3.720	5.07	1.24
6	212.4	0.579	3.68	9.07×10^{-3}	3.716	4.23	1.04
8	209.2	0.481	3.06	7.65	3.712	3.51	8.78×10^{-3}
10	205	0.399	2.54	6.47	3.708	2.91	7.42
12	201.4	0.330	2.10	5.45	3.703	2.41	6.25
14	197.8	0.2715	1.73	4.57	3.699	1.98	5.24
16	194.6	0.2229	1.42	3.81	3.695	1.63	4.37
18	191.4	0.1825	1.16	3.17	3.690	1.33	3.64
20	188.2	0.1489	9.47×10^{-1}	2.63	3.686	1.09	3.02
22	185.2	0.1211	7.70	2.18	3.686	8.84×10^{-1}	2.50
24	182.5	9.82×10^{-2}	6.25	1.79	3.678	7.17	2.05
26	180	7.95	5.06	1.47	3.673	5.81	1.69
28	177.5	6.41	4.08	1.20	3.669	4.68	1.38
30	175	5.16	3.28	9.81×10^{-4}	3.664	3.76	1.13
32	172.5	4.14	2.63	7.98	3.660	3.02	9.16×10^{-4}
34	170	3.31	2.11	6.48	3.656	2.42	7.44
36	167.5	2.637	1.68	5.24	3.652	1.93	6.01
38	164.8	2.095	1.33	4.23	3.648	1.53	4.86
40	162.4	1.660	1.06	3.40	3.643	1.22	3.90
42	160	1.310	8.33×10^{-2}	2.72	3.638	9.56×10^{-2}	3.12
44	158	1.032	6.56	2.17	3.634	7.53	2.49
46	156	8.10×10^{-3}	5.15	1.73	3.630	5.91	1.99
48	154.1	6.34	4.03	1.37	3.626	4.63	1.57
50	152.2	4.95	3.15	1.08	3.622	3.62	1.24
52	150.3	3.86	2.45	8.54×10^{-5}	3.618	2.81	9.80×10^{-5}
54	148.7	2.99	1.90	6.69	3.614	2.18	7.68
56	147.2	2.319	1.47	5.24	3.609	1.69	6.01
58	145.7	1.792	1.14	4.09	3.605	1.31	4.69
60	144.2	1.382	8.79×10^{-3}	3.19	3.601	1.01	3.66
62	143	1.063	6.76	2.47	3.597	7.76×10^{-3}	2.84
64	142	8.17×10^{-4}	5.20	1.91	3.592	5.97	2.19
66	141	6.26	3.98	1.48	3.588	4.57	1.70
68	140	4.79	3.04	1.14	3.584	3.49	1.31
70	139.5	3.67	2.33	8.75×10^{-6}	3.580	2.67	1.00
72	139	2.80	1.78	6.70	3.576	2.04	7.69×10^{-6}
74	139	2.141	1.36	5.12	3.572	1.56	5.88
76	139	1.637	1.04	3.92	3.568	1.19	4.50
78	139	1.252	7.96×10^{-4}	3.00	3.564	9.14×10^{-4}	3.44
80	139	9.57×10^{-5}	6.09	2.29	3.559	6.99	2.63
82	139	7.32	4.66	1.75	3.555	5.35	2.01
84	139	5.61	3.57	1.34	3.551	4.10	1.54
86	139	4.29	2.73	1.03	3.547	3.13	1.18
88	139	3.29	2.09	7.87×10^{-7}	3.543	2.40	9.03×10^{-7}
90	139	2.518	1.60	6.03	3.539	1.84	6.92
92	139	1.929	1.23	4.62	3.535	1.41	5.30
94	139	1.479	9.41×10^{-5}	3.54	3.531	1.08	4.06
96	139	1.134	7.21	2.71	3.527	8.28×10^{-5}	3.11
98	139	8.70×10^{-6}	5.53	2.08	3.523	6.35	2.39
100	139	6.67	4.24	1.60	3.519	4.87	1.84

where $\mu = 43.49$, $R = 191.18$ joul/kg K, gravity $g(z)$, and temperature $T(z)$ values at altitude z can also be found in Table 3-1. A plot of the modeled pressure profile is given in Figure 3-1. The pressure decreases in the model by five orders of magnitude from the surface up to 100 km.

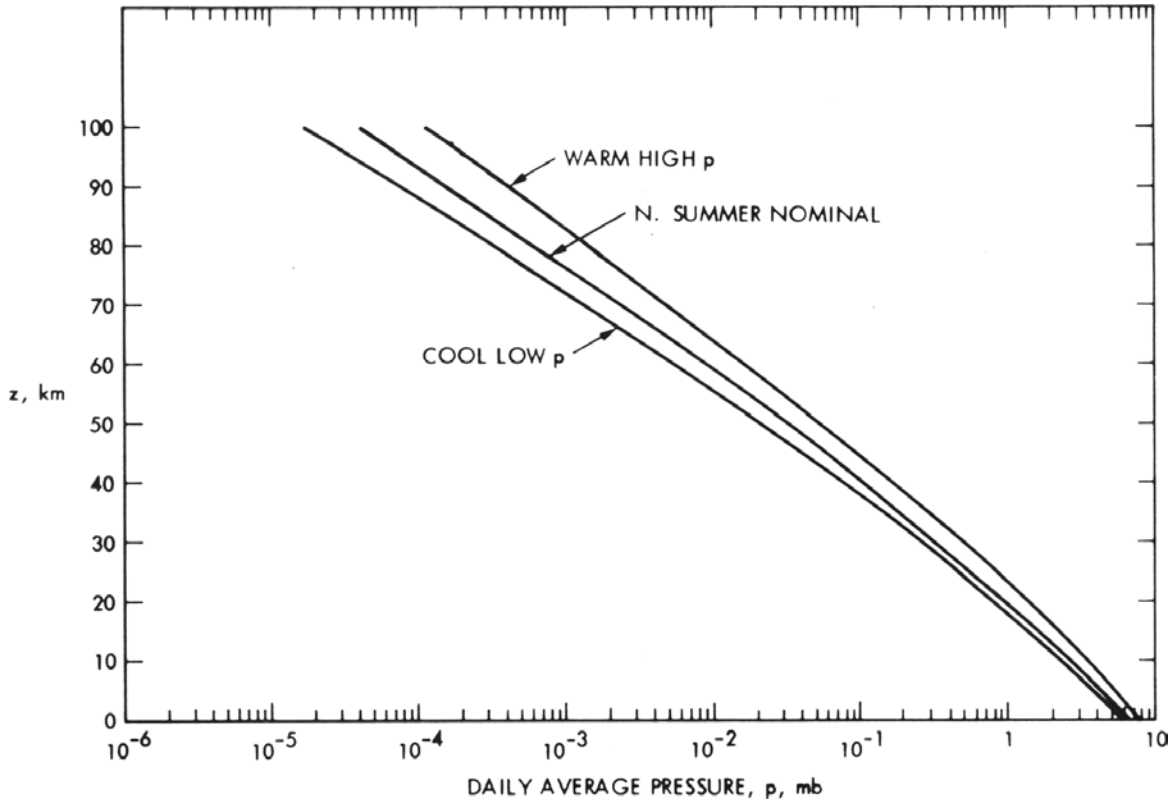

Figure 3-1. Nominal Northern Summer Mid-Latitude Model of the Atmosphere of Mars and Variation of Warm and Cool Summer (from Seiff, 1982).

3.2 Martian Tropospheric Effects

The Martian atmospheric refractive index governs the propagation of radio waves. The index is a function of the atmospheric pressure and temperature, as shown in Equation (1-3). To understand variations of the index, we need to study both Martian atmospheric pressure and temperature. The atmosphere of Mars is much thinner than that of Earth, with a surface pressure averaging 1/100th that at the surface of the Earth. Barometric pressure varies at each landing site on a semi-annual basis. When the southern cap is largest, the mean daily pressure observed by Viking Lander 1 was as low as 6.8 millibars (mb); at other times of the year, the observed pressure was as high as 9.0 mb. The pressures at the Viking Lander 2 site were 7.3 and 10.8 mb (730 and 1080 Pa). In comparison, the average pressure of the Earth is 1013 mb (1.013×10^5 Pa).

Figure 3-2 shows one of the latest atmospheric pressure profiles measured by MGS occultation from the Martian surface to 45-km altitude [Hinson et al., 1999]. The pressure was measured at the local time of 0535 a.m. and in late fall. In this particular instance the pressure was 6.3 mb at the 0-km altitude, even though the 0-km altitude is defined as the reference surface where the atmospheric pressure averages 6.1 mb (610 Pa); dust storms often increase the atmospheric

pressure. In November 1997, MGS observed the thermospheric response to the dust storm, increasing the altitude of the thermospheric pressure surface by 8 km at middle north latitude [Keating et al., 1998].

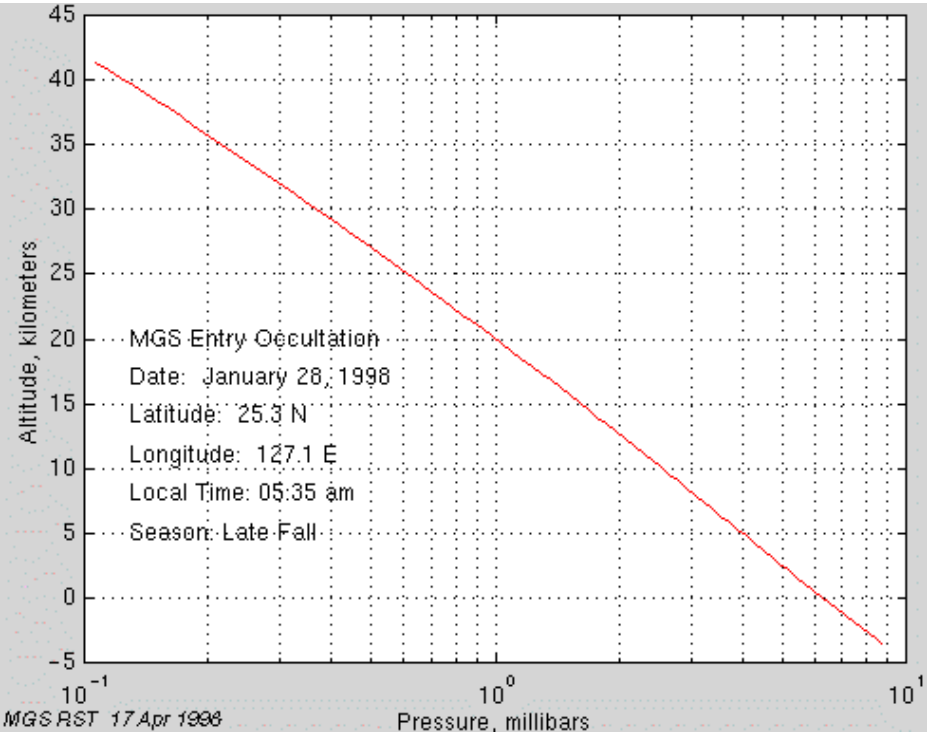

Figure 3-2. Atmospheric Pressure Profile Measured by MGS Radio Occultation on January 28, 1998.

Figure 3-3 shows, respectively, altitude profiles of the atmospheric density (left) and temperatures (right) measured by Mars Pathfinder as it descended through the nighttime atmosphere and landed on the surface [Schofield et al., 1997]. Figure 3-3 shows that near the surface where Pathfinder landed (at night) the temperature was 200 K, in the middle of the atmosphere the temperature was 100 K, and at the uppermost reaches of the atmosphere the temperatures ranged from 150 to 300 K. This uppermost region of the atmosphere is called the exosphere.

Surface temperatures range from 140 K (–133°C) at the winter pole to 296 K (23°C) on the dayside equator during summer. Although the length of the Martian day (24 hours and 37 minutes) and the tilt of its axis (25 degrees) are similar to those on Earth (24 hours and 23.5 degrees), the orbit shape of Mars around the Sun affects the lengths of the seasons the most. Figure 3-4 shows one of atmospheric temperature profiles from MGS occultation measurements [Hinson et al., 1999]. The temperature has a peak value of 218 K (–55°C) at the 10-km altitude.

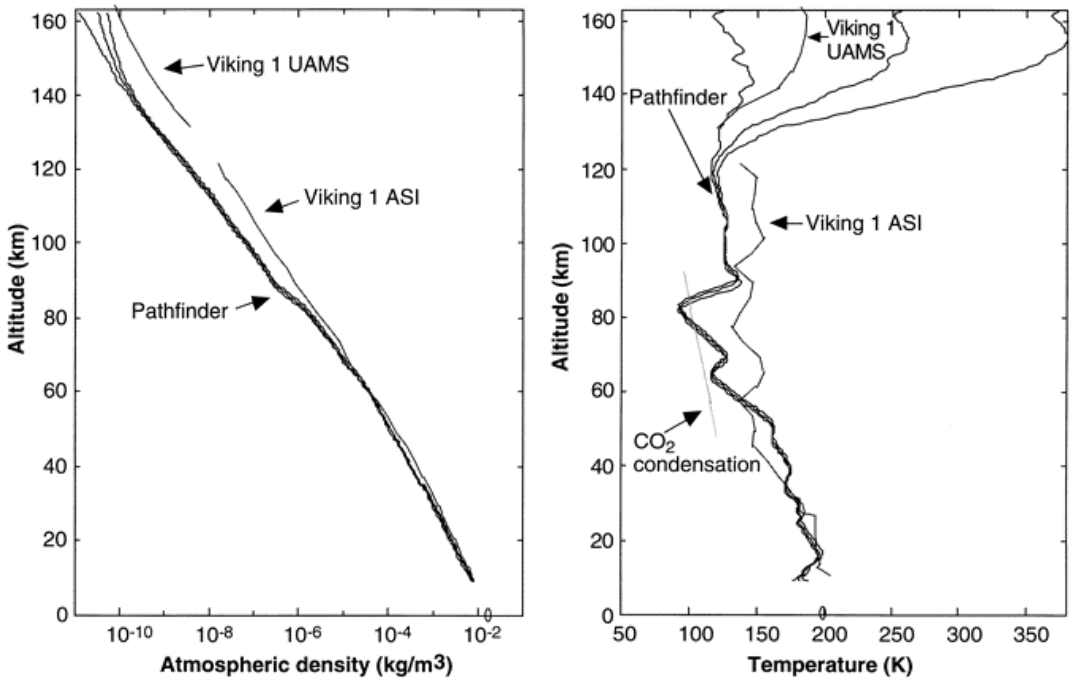

Figure 3-3. (Left) The Atmospheric Density Profiles Derived from the Mars Pathfinder Accelerometer Data. Results from the VL-1 atmospheric structure instrument (ASI) and the Viking 1 upper atmosphere mass spectrometer (UAMS) are also plotted for comparison. (Right) The atmospheric temperature profiles derived from the Pathfinder measurements and from the VL-1 ASI, UAMS experiments, and the CO_2 condensation. The surface density and temperature measured by the Pathfinder MET instrument (oval) are also shown.

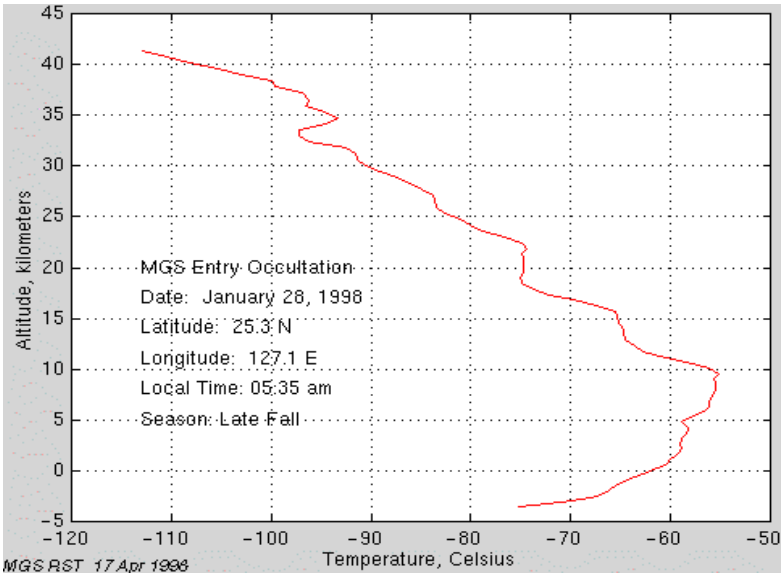

Figure 3-4. Martian Atmospheric Temperature Profile Measured by MGS Radio Occultation on January 28, 1998.

Above an altitude of 10 km, the temperature decreases with height. This is the usual behavior in atmospheres or atmospheric layers. Below 10 km, however, the temperature increases with height. This is called a temperature nighttime inversion. In this case, the inversion results from the radiation of infrared energy from the surface of Mars and the atmosphere in close contact with it, which occurs through the night hours [Hinson et al., 1999]. The loss of energy leads to cooling. The same phenomenon takes place here on Earth on clear nights with little or no wind. Radiation inversions generally dissipate in the hours after the Sun rises and the surface is warmed once again.

The Viking Lander meteorological sensors gave detailed information about the atmosphere. They found patterns of diurnal and longer-term pressure and temperature fluctuations. The temperature reached its maximum of 238 K every day at 2 p.m. local solar time and its minimum of 190 K just before sunrise. Local time changes in the temperature profiles in the lowest 8 km are modeled in Figure 3-5. In the lowest 4 km, there is a boundary layer that is strongly influenced by radiative exchange with the ground and in which an intense nighttime inversion forms. On Mars, the atmospheric pressure varies with the seasons. During winter, it is so cold that 20 to 30 percent of the entire atmosphere freezes out at the pole, forming a huge pile of solid carbon dioxide. The pressure minimum of just under 6.7 mb (roughly 0.67 percent of pressure at Earth sea level) was reached on sol 100, the 100th Martian day after the Viking 2 landing, as shown in Figure 3-6. The pressure minimum seen by Pathfinder indicates that the atmosphere was at its thinnest (and the south polar cap probably its largest) on sol 20.

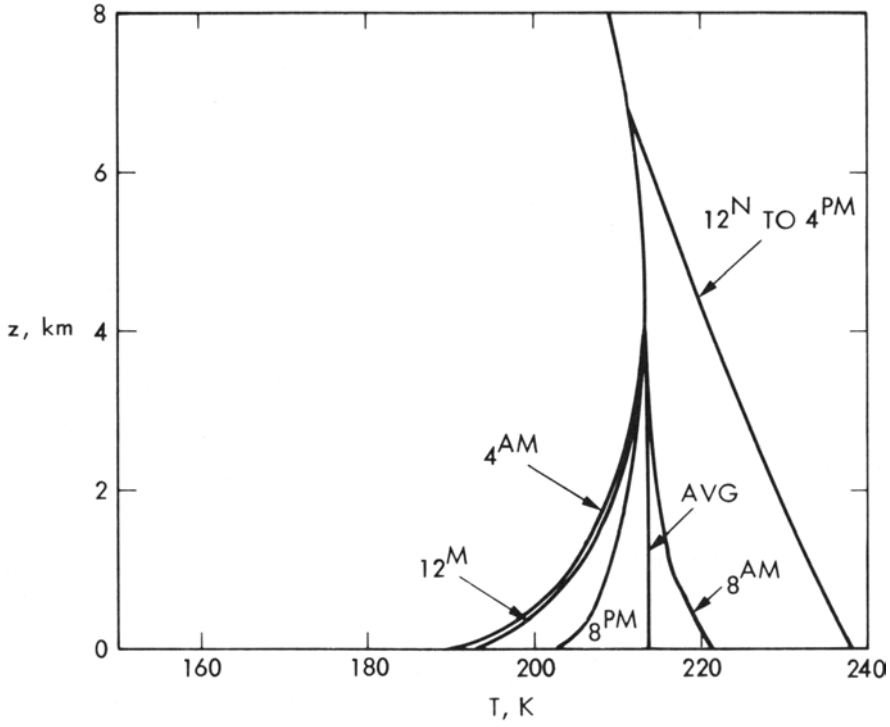

Figure 3-5. Models of Martian Atmospheric Surface Temperature Variation and Temperature Profiles in the Lowest 8 km (Seiff, 1982).

Morning temperatures fluctuated abruptly with time and height. The Viking sensors positioned at 0.25, 0.5, and 1 m above the surface obtained different readings. This suggests that cold morning air is warmed by the surface and rises in small eddies, or whirlpools; this is very different from what happens on Earth. Afternoon temperatures, after the atmosphere had warmed, did not show the same variations. In the early afternoon, dust devils repeatedly swept across the lander. They showed up as sharp, short-lived pressure changes, and they were probably similar to events detected by the Viking landers and orbiters. Such dust devils may be an important mechanism for raising dust into the Martian atmosphere. The prevailing winds were light (less than 10 m/s, or 36 km/hr) and variable.

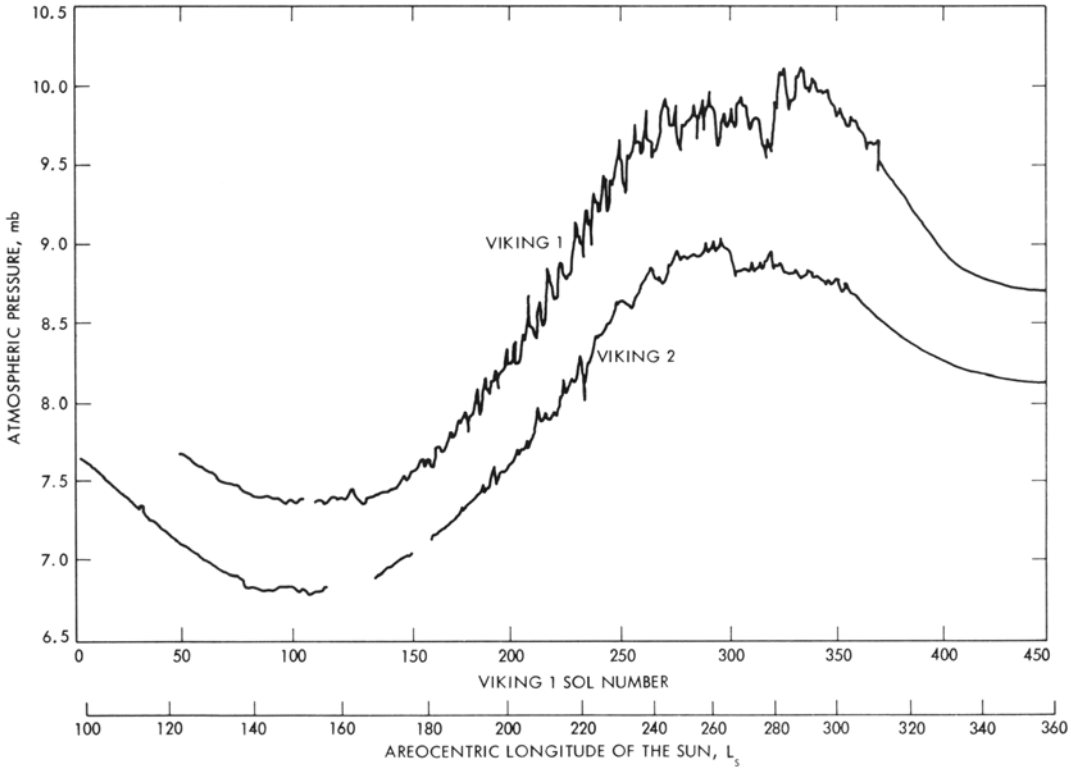

Figure 3-6. Seasonal Variation of Surface Pressure at the Two Viking Sites (Leovy, 1982).

Mars Pathfinder measured atmospheric conditions at higher altitudes during its descent. The upper atmosphere (above 60-km altitude) was colder than Viking had measured. This may simply reflect seasonal variations and the time of entry: Pathfinder came in at 3 a.m. local solar time, whereas Viking arrived at 4 p.m., when the atmosphere is naturally warmer. The lower atmosphere was similar to that measured by Viking, and its conditions can be attributed to dust mixed uniformly in comparatively warm air.

Two major effects of the Martian troposphere on radio wave propagation are probably multipath (due to the refraction) and scintillation (due to irregularities). Other effects in a clear Martian atmosphere (such as fading, dispersion, etc.) are neglected. Because Martian atmospheric pressure and temperature vary with altitude, vertical gradients exist in the refractive index in the troposphere (lower atmosphere). This causes multipath effects for radio waves with different

launch angles due to ray bending. When a radio ray is not launched exactly vertically (perpendicular to the gradient), it gradually changes its direction, sometimes even going back to the Martian surface. Since the refractive index varies mainly with altitude, only the vertical gradient of the refractive index n [Bean and Dutton, 1966] is considered in most cases. The bending of a ray at a point is expressed by

$$\frac{1}{\rho} = \frac{\cos\varphi}{n}\frac{dn}{dh} \tag{3-3}$$

where ρ is radius of curvature, dn/dh is vertical gradient of the refractive index, h is height of the point above the Mars surface, and φ is the angle of the path relative to the horizontal of the point considered.

Only when a wave's launch angle is near 0° (close to horizontal) can the ray be trapped in a horizontal ducting layer. Because $n \approx 1$, from equation (3-3), we have an approximation

$$\frac{1}{\rho} = \frac{dn}{dh} = 10^{-6}\frac{dN}{dh} \tag{3-4}$$

where radio refractivity $N = (n-1)\times 10^6 = 130.6P/T$ (N unit) from Equation (1-4), P is atmospheric pressure (in mb), and T is temperature (in Kelvins) for a dry atmosphere (Martian atmospheric water vapor pressure is neglected here). Based on the altitude profiles of Martian atmospheric P and T shown in Figures 3-4 and 3-5, we have calculated and plotted the altitude profile of the radio refractivity N in Figure 3-7. This profile can be fitted using a function

$$N(h) = N_0 \exp(-h/H_N) \tag{3-5}$$

where N_0 is the surface value of N when altitude h = 0, and H_N is the refractivity scale height. From the best fitting, we can find that N_0 = 3.9 (N unit) at Martian surface and H_N = 11.0 km. We also have

$$dN/dh = -N(h)/H_N \tag{3-6}$$

Because the Martian atmosphere has a very small N (only 1.2% of the Earth's, 315 N unit) and also a very small gradient dN/dh, there will be very small ray-bending effects. Only when the wave angle is very close ($\varphi < 0.3°$) to the horizon, can the wave ray be trapped by a horizontal duct (surface or elevated). Temperature changes near the surface have little effect on the N. For example, a 20°C change in temperature detected by Viking 1 and 2, as shown in Figure 3-8, only makes a contribution of 0.22 N unit (about 10%) to N. Even through the ray-bending effect is small, exact phase delays, range delays, and appearing angle deviations need to be calculated. When the wave propagates nearly horizontally and is trapped in a surface duct, it bounces back inside the waveguide between the Martian surface and the top reflection layer. Because Mars is only about half the size of Earth and because Mars has a larger surface curvature than Earth, it is expected that the signals will have a greater defocusing loss.

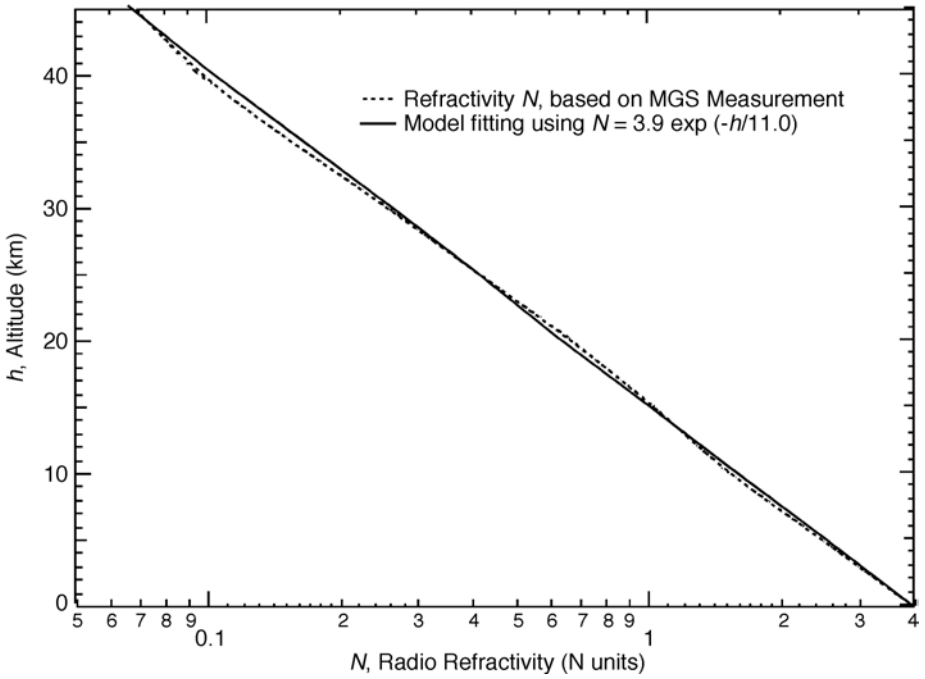

Figure 3-7. Radio Refractivity for Martian Atmosphere. Dry air pressure and temperature profiles are used for the refractivity calculation.

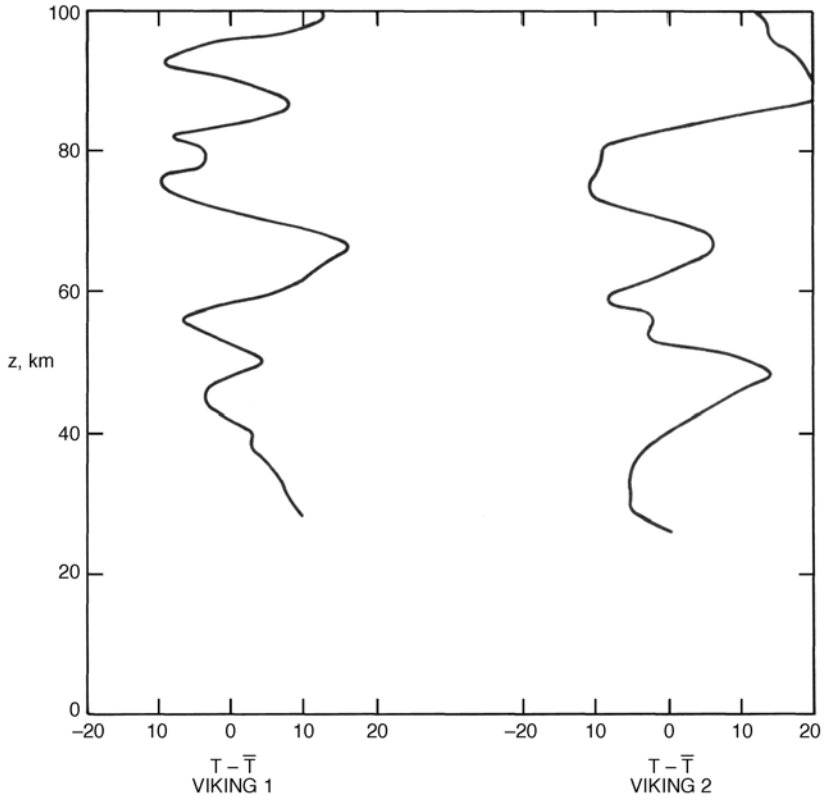

Figure 3-8. Temperature Oscillations Found in the Viking Temperature Soundings (from Seiff, 1982).

Tropospheric scintillation is caused by turbulence-induced spatial and temporal refractive index variation. Refractive index variations also cause wavefront distortions and increase the bit- error rate. Tropospheric scintillation caused by refractive index irregularities has been observed on Earth space paths at frequencies to above 30 GHz.

It is hard to determine from available Mars data the extent of Martian tropospheric turbulence and irregularities. However, refraction index theories developed for Earth's atmosphere can be applied to the Martian atmosphere. There is a relation between the size of the mean square fluctuations of the refractive index C_N and the size of the mean square fluctuations of temperature C_T [Annis, 1987]:

$$C_N \propto \frac{P}{T^2} C_T \tag{3-7}$$

where T and P are temperature and pressure in the Martian troposphere. The ratio of Mars to Earth in fluctuations is

$$\frac{C_{N,Mars}}{C_{N,earth}} = \frac{P_{Mars}}{P_{Earth}} \left(\frac{T_{Earth}}{T_{Mars}} \right)^2 \frac{C_{T,Mars}}{C_{T,Earth}} \approx 0.5\% \frac{C_{T,Mars}}{C_{T,Earth}} \tag{3-8}$$

Thus, refraction index variation fluctuations in Martian troposphere should be only about 0.5% of that in the Earth atmosphere, if C_T is the same for Mars and Earth.

3.3 Martian Clouds and Fogs

The Martian atmosphere contains only a very small amount of water (0.03% by volume, which is 1/300 to 1/1000 as much water as Earth). However, because of low pressure and temperature, the water can still condense out to form clouds in the atmosphere. Unlike the Earth, where clouds are found around the entire globe, on Mars, clouds seem to be plentiful mainly below the middle latitude region, as shown in the Hubble telescope image in Figure 3-9. Many of the cloud formations seem to be due to topographic forcing by Olympus Mons. This may be because water on Mars is mainly found around the equator and low latitudes. Recent detailed pictures from MGS have revealed many young gullies, possibly formed by flowing water, at the Martian surface between latitudes 30° and 70°. Because the Martian surface atmospheric pressure is so low, the water must be quickly evaporated or go underground [Malin and Edgett, 2000].

As early as 1796 scientists were reporting "yellow" clouds and "white" or "bluish" clouds in the Martian atmosphere. However, it wasn't until the Mariner 9 mission that clouds of water were positively identified. Mars Global Surveyor is providing more proof of the existence of water clouds. Using its thermal emission spectrometer, MGS detected water in some clouds. Mars Pathfinder took images of Martian clouds from the ground level. A few clouds have been seen at the north pole [Briggs et al., 1977]. This may have been because the north polar ice cap was evaporating with the coming of the northern spring season.

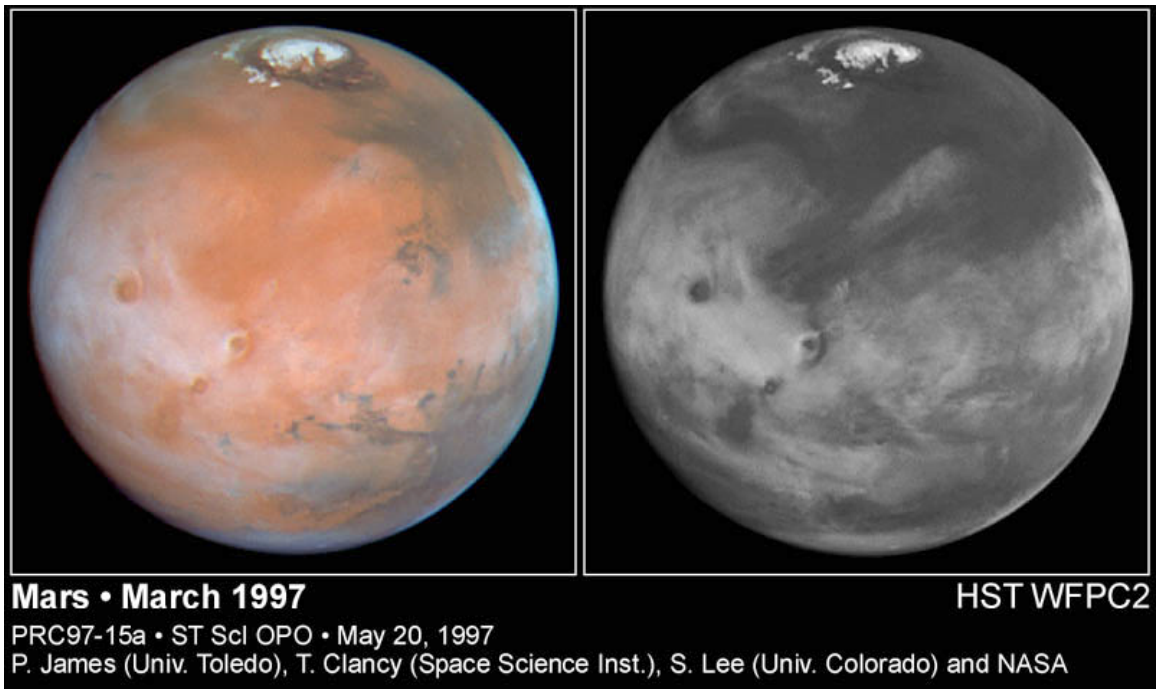

Figure 3-9. A Hubble Telescope Image of Martian Clouds. The clouds are found mostly in the equatorial and low latitude regions.

In the Earth atmosphere, rain droplets have larger particle sizes than water particles in clouds and fogs (< 0.01 cm). Thus, Rayleigh scattering theory applies. There is a general relation between the wave attenuation and total water content per unit volume for Rayleigh scattering.

$$\alpha_c = k_i \rho_l \tag{3-9}$$

where α_c is the specific attenuation (dB/km) within clouds, k_i is the attenuation coefficient (dB/km/gm/m^3) determined from Rayleigh scattering theory, and ρ_l is water content (g/m^3). The total cloud attenuation can be obtained by computing the total content of water along the path. Based on Rayleigh scattering, the coefficient k_i is a function of dielectric permittivity ε and relative dielectric permittivity K_c for frequencies up to 100 GHz, as shown below.

$$k_i = 0.4343 \frac{6\pi}{\lambda} Im\left[-\frac{K_c - 1}{K_c + 2}\right] \tag{3-10}$$

where λ is the wavelength, *Im* indicates the imaginary part of K_c, and K_c is the complex relative dielectric permittivity of water or ice (that is dielectric permittivity $\varepsilon = \varepsilon_0 K_c$, where ε_0 dielectric permittivity at free space). The quantity K_c is a function of temperature and frequency.

Cloud drop sizes, liquid water content, relative dielectric permittivity K_c, and the coefficient k_i for the Earth atmosphere are well documented in the studies of Gunn and East [1954], Battan [1973], Ludlam [1980], and Slobin [1982]. Table 3-2 shows values of the imaginary part of $-(K_c - 1)/(K_c + 2)$, adapted from Battan [1973]. Values of attenuation coefficient k_i by water and ice clouds were calculated by Gunn and East [1954] for various wavelengths at various temperatures and are given in Table 3-3. These values can provide an upper limit for Martian cloud attenuation.

Table 3-2. Values for Complex Relative Dielectric Permittivity of Water Ice *Im* $[-(K_c - 1)/(K_c + 2)]$ (adapted from Battan, 1973)

Substance	*T* (°C)	$\lambda = 10$ cm	$\lambda = 3.21$ cm
Water Ice	0°	9.6×10^{-4}	9.6×10^{-4}
Water Ice	–10°	3.2×10^{-4}	3.2×10^{-4}
Water Ice	–20°	2.2×10^{-4}	2.2×10^{-4}

Table 3-3. One-way Attenuation Coefficient, k_i in Clouds (dB/km/g/m^3)

Temperature	Wavelength (cm)			
K (°C)	0.9	1.24	1.8	3.2
Water Ice 273 (0)	8.74×10^{-3}	6.35×10^{-3}	4.36×10^{-3}	2.46×10^{-3}
Cloud 263 (–10)	2.91×10^{-3}	2.11×10^{-3}	1.46×10^{-3}	8.19×10^{-4}
253 (–20)	2.0×10^{-3}	1.45×10^{-3}	1.0×10^{-3}	5.63×10^{-4}

From the tables, we can see that attenuation decreases with increasing wavelength. For signals with frequencies of 10 GHz and lower, attenuation due to clouds is small. Values of *Im* $[-(K_c - 1)/(K_c + 2)]$ for ice clouds are independent of wavelengths.

At Earth, for signals with frequencies below 100 GHz, fog attenuation is not significant. Medium liquid fog typically has a water content of about 0.05 gm/m^3 and a visibility (V) of 300 m. This causes a 0.4-dB/km attenuation for a radio wave with a frequency of 140 GHz. The attenuation for a thick fog ($\rho_l = 0.5$ gm/m^3 and $V = 50$ m) is 4 dB/km. In additional to the cloud attenuation, clouds also can increase the system noise temperature because clouds are a source of emission as well as absorption [Slobin, 1982].

Because of the very low temperatures, Martian clouds probably consist of ice crystals. Some clouds may consist of CO_2 droplets. Radio wave attenuation due to ice clouds is two orders of magnitude smaller than that of water clouds, but water clouds have a strong depolarization effect on radio waves. For the Martian atmospheric cloud attenuation study, the problem is that at this stage we do not know what percentage of Martian clouds consist of water liquid or ice and what percentage are CO_2 clouds. We also do not have any direct measurement of water content within the clouds. An alternative way to calculate the scattering attenuation due to cloud and fog on radio waves is to use the observed optical depth through the following relation:

$$A(\lambda) = 54.62 \frac{r\tau}{\lambda} \left[\frac{3\varepsilon''}{(\varepsilon'+2)^2 + \varepsilon''^2} \right] \tag{3-11}$$

where $A(\lambda)$ is attenuation in dB/km, τ is optical depth, r is the particle radius in meters, λ is the wavelength in meters, and ε' and ε'' are the real and imaginary parts of the mean permittivity of the cloud droplets. The optical depth, τ, is a measure of attenuation over the entire path taken from the ground to space. Optical depth increases as the line of sight moves down toward the horizon because of increasing path length. The optical depth may be obtained through the following measurements. The power received, P_r, is the power transmitted, P_t, multiplied by the attenuation: $P_r = P_t e^{-\tau}$ (i.e., $\tau = ln(P_t / P_r)$.

There is a distinct seasonal dependence as well as a latitude dependence for Martian cloud distributions. A longitudinal dependence and a time-of-day dependence are not obvious. Some Martian clouds form at dawn and burn off rapidly, and others form only in midday. In general, the northern hemisphere is covered with more clouds than the southern hemisphere [Kahn, 1984]. Clouds are relatively abundant during northern spring and summer at mid-latitudes. In the southern hemisphere the situation is complicated by atmospheric dust. Overall, the Martian clouds have an optical depths of 0.05–3.0, a figure closer to terrestrial thin and high-level cirrus clouds (τ = 0.5–3.5). For comparison, a terrestrial stratus cloud has an optical depth of ~ 6–80, while a cumulus cloud has an optical depth of ~ 5–200. It should be mentioned that these optical depths are at visual wavelengths (0.67 microns).

More study is needed to understand just how clouds are formed in the Martian atmosphere. For example, even though clouds have been found, we still do not know whether there is rain on Mars. Atmospheric temperatures reported by Mars Pathfinder during its descent indicate that it may be too cold in the cloud-forming region of the Martian atmosphere for droplets to fall to the ground as liquid, but it may be cold enough for the condensation of CO_2 droplets.

To answer these questions, 58,000 images of Mars provided from Viking Orbiters and Mariner 9 have been analyzed. Cloud distributions with seasons and latitudes have been obtained [Kahn, 1984; Thorpe, 1977]. Mars Pathfinder took measurements of many clouds in the Martian sky from the surface of Mars itself. The images of the Martian sky from the 80-day mission provided further assessment of Martian weather patterns.

Widespread thick clouds mainly occur in three regions: the polar hoods, the Tharsis bulge, and the plateau region in the southwestern end of the Marineris valley. These clouds usually have thinner optical depths ~0.05. Isolated clouds include the following:

1. Lee waves. These clouds form in the lee of large obstacles such as mountains, ridges, craters, and volcanoes.
2. Wave clouds. These clouds appear as rows of linear clouds. They are common at the edge of the polar caps.
3. Cloud streets. These clouds exhibit a double periodicity. They appear as linear rows of cumulus-like, bubble-shaped clouds.
4. Streaky clouds. These clouds have a preferred direction without periodicity.

5. Plumes. These are elongated clouds. They appear to have a source of rising material and in many cases are composed of dust particles.

As a summary, we list optical depths for both Earth and Mars cloud patterns in Table 3-4.

Table 3-4. Visual Optical Depths of Clouds and Fogs on Earth and Mars*

Atmospheric Condition	Earth		Mars	
	Optical Depth	Distribution	Optical Depth	Distribution
Clouds H_2O	~5	50% coverage	~1.0	Winter polar; behind high places
Clouds CO_2	None	None	~0.001 ~1.0	Many places Winter polar
Fog	~3	Many places	~0.2 ~1.0	Morning Valleys & crater bottoms
Aerosol Dust	Variable	Variable	0.5	Everywhere
Dust Storms	Variable	Variable	10.0	Southern Hemisphere or global

*Adapted from Annis [1987].

Martian fog usually occurs in low areas such as valleys, canyons, and craters. It forms during the coolest times of the day, such as dawn and dusk [Annis, 1987]. The fog seems to burn off in the afternoon. Fog seen by the Viking Landers was thin, about $\tau = 0.2$. Sometimes Martian ground haze is caused by dust in the atmosphere; however, if the atmosphere is clear, ground fog can be easily identified.

Using the optical depths listed in Table 3-4 and Equation (3-11) for a given droplet radius and permittivity, we can calculate the wave attenuation for various wavelengths. It is believed that the total attenuation for Ka-band radio wave signals is about 0.1 dB.

3.4 Martian Aerosols

It is believed that Martian dust particles are the main contribution to the Martian aerosols. The Martian sky appears pink and somewhat dark at sunset. This is because there are not enough molecules in the atmosphere to scatter the amount of light we are used to seeing on Earth. Also, the many rust-colored dust particles in the atmosphere contribute to the pink color.

Mars Pathfinder found that the sky on Mars had the same pale pink color as it did when imaged by the Viking landers [Golombek et al., 1997; Schofield et al., 1997]. Fine-grained, bright-red dust in the atmosphere would explain this color. This suggests that the Martian atmosphere always has some dust in it from local dust storms. The inferred dust-particle size (roughly a micron), shape, and amount of water vapor (equivalent to a meager one-hundredth of a millimeter of rainfall) in the atmosphere are also consistent with measurements made by Viking.

On Mars, the dust intercepts essentially the same amount of sunlight in all colors. The reddish color of the sky is produced when the blue light is absorbed by the dust, but the red light is scattered throughout the sky.

It is not clear if Martian hazes are due to dust or ice. They have optical depths on the order of 1, although they can sometimes can be greater than one [Christensen and Zurek, 1984]. Viking 1 found a background haze of $\tau \sim 0.3$, while Viking 2 found a similar haze of $\tau \sim 0.5$. The optical depth for Martian dust aerosols is 0.5 as listed in Table 3-4. As a comparison, Martian dust storms have much higher optical depths. Viking Lander 1 measured higher optical depths of $\tau =$ 2.7 and 3.7 for two global storms [Tillman et al., 1979]. Pollack et al. [1977 and 1979] estimated an upper limit on those dust storms of $\tau = 3.7$ and 9, respectively.

A dust devil is a swirling, vertical updraft of air developed by local heating of the air above a flat desert floor. Pathfinder detected several signatures of a dust devil that passed over the lander on Sol 25 [Schofield et al., 1997]. Over a period of approximately two minutes, the surface pressure showed a sharp minimum approximately 0.5% below the background pressure. The East wind increased suddenly as the dust devil approached the lander, and the pressure began to fall. As the dust devil passed over the lander, pressure began to rise, the East wind died away, and the West wind increased suddenly. Finally, as the dust devil moved away, pressure returned to normal, and the West wind died away. This is a textbook dust-devil signature. The motion direction of the dust devil relative to the Pathfinder in terms of wind speed and surface pressure is schematically shown in Figure 3-10.

The Pathfinder's Rover measured the dust deposited on the Rover's solar array by measuring the change in transparency of a movable glass cover as dust settled on it [Rieder et al., 1997; Team, 1997]. The Rover solar array was found to be accumulating dust at a rate of about a quarter of a percent of coverage per day. This is very close to the coverage of 0.22% predicted [Landis, 1996]. The deposition rate seems to be the same on the sols when the Rover was in motion as it was on sols when the Rover remained in place, indicating that the deposition was probably due to dust settling out of the atmosphere, not dust kicked up by the rover's motion.

Mars Pathfinder produced the following findings about dust aerosols [Schofield et al., 1997; Team, 1997]:

1. Martian dust included magnetic composite particles with a mean size of one micron.
2. The observed atmospheric clarity was higher than was expected from Earth-based microwave measurements and Hubble Space Telescope observations.
3. Dust was confirmed as the dominant absorber of solar radiation in the Martian atmosphere, which has important consequences for the transport and circulation of energy in the atmosphere.
4. Frequent "dust devils" were found with an unmistakable temperature, wind, and pressure signature, and with morning turbulence; at least one may have contained dust (on Sol 62), suggesting that these gusts are a mechanism for mixing dust into the atmosphere.

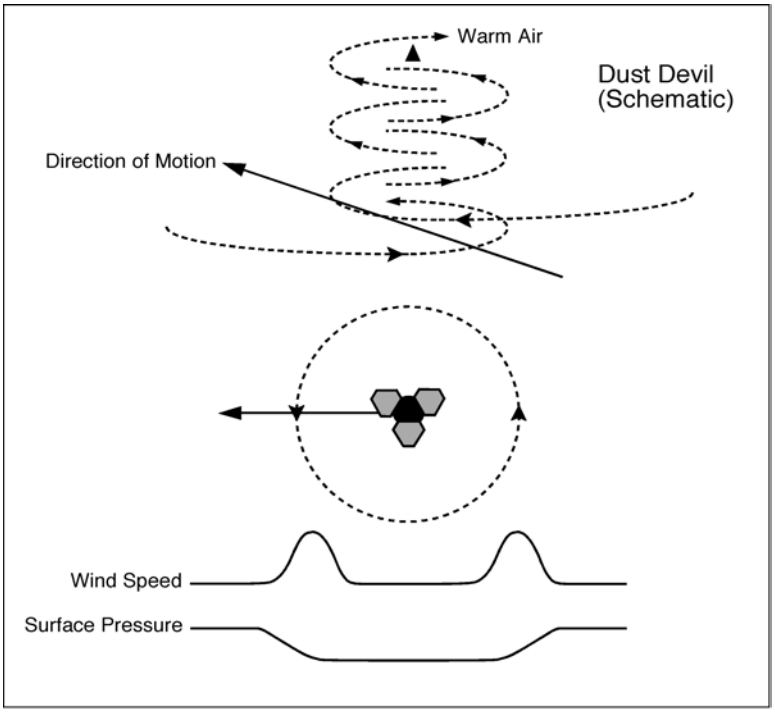

Figure 3-10. Simplified Schematic Drawing of the Dust Devil That Passed Over the Sagan Memorial Station (Mars Pathfinder) on Sol 25. It shows direction of motion and the graphs of a textbook dust devil in terms of wind speed and surface pressure.

It is expected that total attenuation at Ka-band due to Martian dust aerosols is less than 0.1 dB along a vertical path.

3.5 Communication Blackout During Atmospheric Entry Phase

When a high-speed (supersonic) spacecraft enters the Martian atmosphere, because its flight speed is much greater than the local speed of sound, a shock layer is formed in the front of the capsule body. The plasma results from thermal ionization of the constituents of the air as it is compressed and heated by the strong bow shock or heated within the boundary layer next to the surface. Because the plasma density surrounding the capsule is very high, communications are disrupted during the entry phase. This phenomenon is usually known as a blackout. In the 1960s during the Apollo Moon mission period, NASA conducted much research and many experiments for Earth atmospheric reentry [Tischer, 1963; Cuddihy et al., 1963; Huber, 1965; Olte, 1966; Mitchell, 1967; Dunn, 1970]. For the manned Apollo mission, the interaction of the high-speed capsule with the dense Earth atmosphere caused a communications blackout duration of 4 to 10 minutes at X-band. During this period, it was not known whether the capsule was destroyed or had just lost contact. Recent literature reflects the lack of ongoing research. Actually, this type of problem has never been completely analyzed [Chadwick, 1997].

The main cause of blackout is reflection or absorption of electromagnetic wave energy at all communication frequencies (f) lower than the local plasma frequency (f_p), where f_p (MHz) = 9.0×10^{-3} $N^{1/2}$ (cm^{-3}). For $f < f_p$ a plasma behaves like a conductor, while for $f > f_p$ the plasma is

practically transparent. The critical plasma densities for various frequencies of signals from UHF to Ka-band are listed in Table 3-5.

Table 3-5. Critical Plasma Densities and Communication Frequencies

Signal Frequency	UHF 381 MHz	S-band 2.295 GHz	X-band 8.43 GHz	Ka-band 32 GHz
Plasma Density	1.8×10^{9} cm^{-3}	6.5×10^{10} cm^{-3}	8.8×10^{11} cm^{-3}	1.27×10^{13} cm^{-3}

Although the Martian atmosphere is very tenuous compared to Earth's atmosphere, the heat generated at the hypersonic entry velocity of 7.0 km/s due to the atmospheric drag can be substantial, and subsequent ionization of some of the atmospheric gases may occur. Therefore, a shock-induced envelope of ionized gases (i.e., a plasmasheath) may form around and trail the capsule as it descends through the Martian atmosphere.

There is no simple solution for the plasma density distribution around the capsule because this process involves complicated chemical reactions. The production rate of electrons due to the impact is a function of spacecraft speed, capsule shape, atmospheric density, and atmospheric composition. Thus, the severity of the attenuation will depend largely on the capsule entry trajectory and altitude profiles of velocity, atmospheric density, and composition. Behind strong normal shock waves, the predominant electron production processes are multi-body atom-atom ionizing collision, photoionization, electron impact, atom-molecule collisions, and molecule-molecule collisions [Lin and Teare, 1963]. The resultant electron concentration also depends on entry angle and attack angle. Vertical incidence (90°) usually generates a great deal of ionization, while a small entry angle (near horizontal motion) causes weaker ionization.

In general, there are two distinctly different plasma regions around a capsule during its impact ionization period, as shown in Figure 3-11. The outer plasmasheath region (between the shock wave and the free shear boundary layer) consists of inviscid air, which is compressed and heated by a strong bow shock wave, producing free electrons. When this fluid expands around the capsule, some of the electrons and ions recombine, but the flow is never in complete thermodynamic and chemical equilibrium [Huber, 1965; Grose et al., 1975]. The inner plasma region (between the free shear layer and the rear body surfaces) is one of separated fluid, which is composed of boundary layer air "contaminated" with ablation material from the heat shield. This air mixture recirculates in the base flow region and is finally scavenged into the wake. There is a higher electron density in the stagnation region (front nose) where electrons are produced, while there is a low plasma density in the rear wake region of the capsule where the antenna is installed. Thus, the signal propagation from an antenna on the body will be through both the inviscid and the separated regions.

To obtain a numerical solution of plasma density profiles around a capsule, one usually needs to solve the Navier-Stokes equations for non-viscous, or viscous flow with gases in thermochemical equilibrium and nonequilibrium [Boukhobza, 1997; Dunn, 1970, Huber, 1965]. Plasma density calculations also need to include all ion chemical reaction (production and recombination) equations of charge exchanges for all species. Some simplified calculation methods to roughly estimate the plasma effects have been worked out [Tischer, 1962 and 1963].

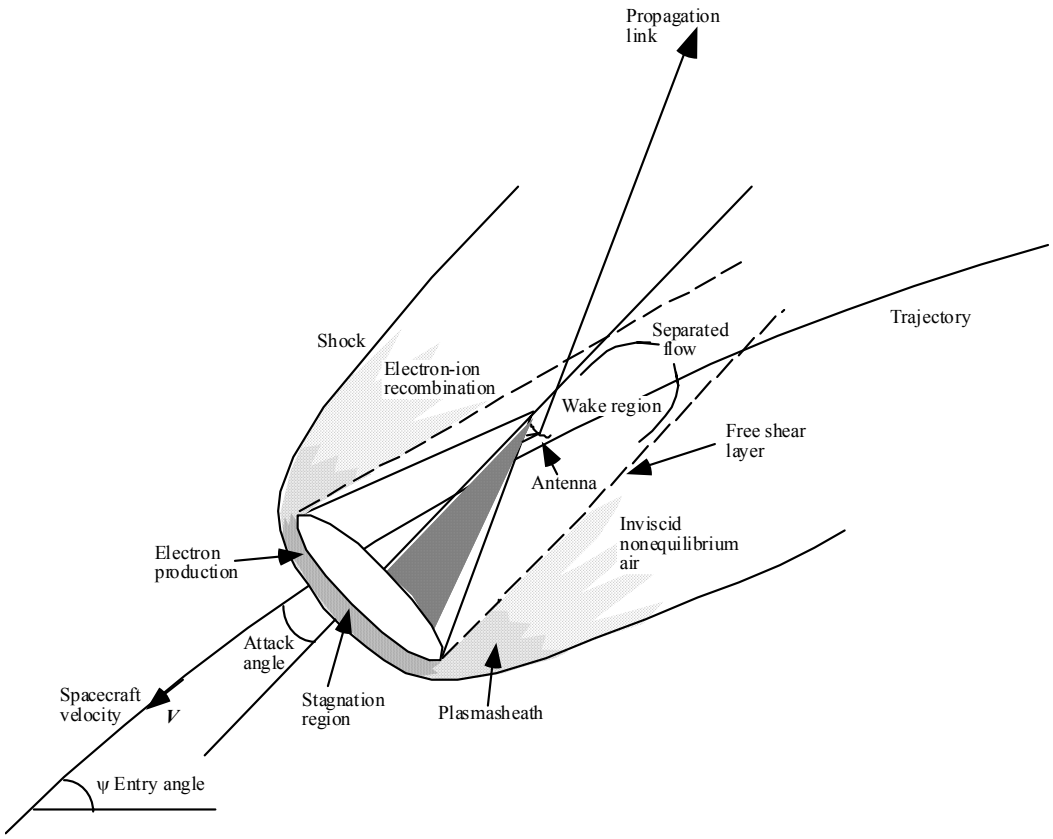

Figure 3-11. Diagrammed View of a Blunt Hypersonic Spacecraft Entering the Martian Atmosphere. A plasmasheath generated around the capsule blacks out the communication signals.

To study the blackout problem caused by atmospheric impacting ionization, JPL developed a computer program to calculate the equilibrium electron density through the thermochemistry and shock heating [Horton, 1964]. The program initializes with a specific gas mixture, temperature, and pressure. For a particular shock velocity, various ion chemical compositions are generated under an equilibrium thermodynamic state. Equations (3-12) and (3-13) below, respectively, represent an empirical fit for the resultant electron density for a shock velocity between 4.0 and 9.0 km/s, at a typical interest range, at stagnation and at the wake region of the capsule.

$$n_{e,s} = 1.5\times10^{10}\,\rho^{0.95}V^{11.8} \text{ at stagnation point} \tag{3-12}$$

$$n_{e,s} = 1.83\times10^{9}\,\rho^{0.95}V^{10.37} \text{ at wake region} \tag{3-13}$$

where ρ is neutral atmospheric mass density in g/cm^3, while V is velocity of the capsule in km/s. Using this computer program and an isothermal Martian atmospheric density profile, Spencer [1964] found the electron density in the wake with a peak value of about 3×10^{12} cm^{-3}. This density is higher than critical density for X-band communication, as shown in Figure 3-12. Using a different Martian atmospheric model, calculations by Nordgard [1976] showed that the electron

density in the wake region of the capsule had a peak value of 7.9×10^{10} cm^{-3}. This is above the critical electron density for the S-band communication links, but it will not black out the X-band transmission link.

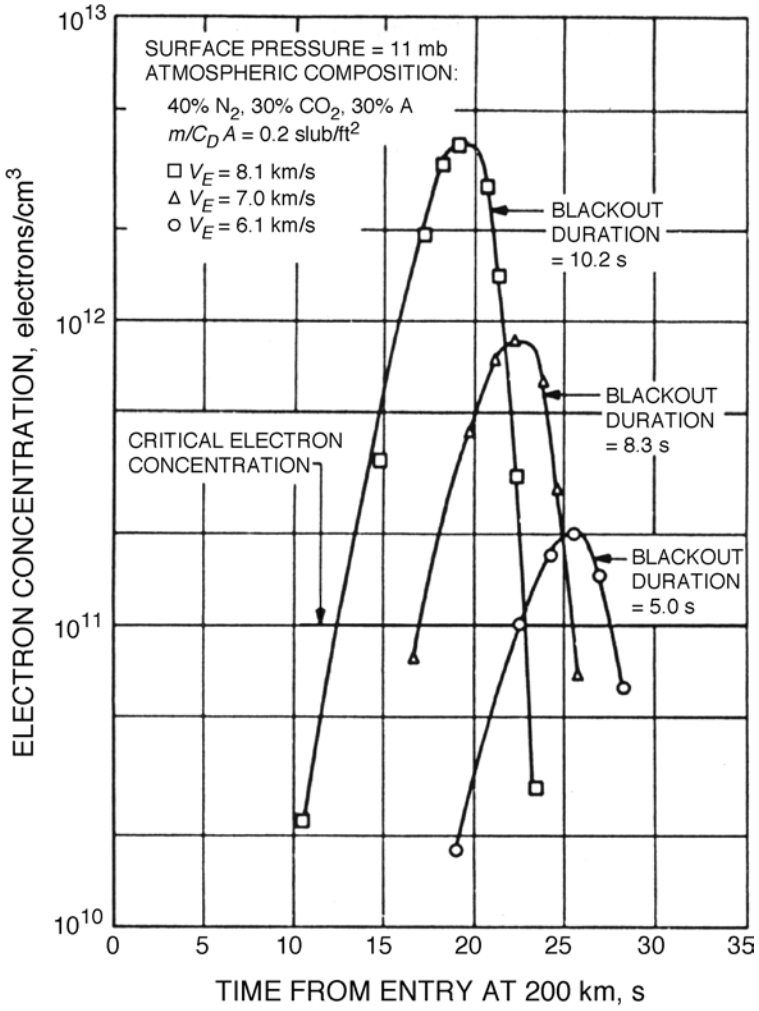

Figure 3-12. Electron Densities in the Capsule Wake Region versus Time from Entry for Various Entry Velocities and for Entry Angle ψ = 90° (from Spencer, 1964).

The Viking I and II landers, the Mars Pathfinder, and future missions (such as Mars 2003) all involve various Martian atmospheric entry projects. The former Soviet Union's Mars 6 experienced a 61-s signal-loss interval at 142.3 MHz, starting from 75-km altitude [Vasilleva et al., 1975]. During the Viking mission, the two Viking landers experienced 1-minute communication blackouts at the UHF band during their EDL phase. On July 4, 1997, the Mars Pathfinder (MPF) spacecraft entered the atmosphere of Mars after a 7-month cruise. The entry speed was approximately 7 km/s. The telecommunication frequency was X-band (8.43 GHz). During descent, signals transmitted from the MPF were extremely dynamic [Wood et al., 1997]. At 125 km in altitude, the MPF speed was 7.6 km/s. The spacecraft used a backshell low-gain antenna to communicate with Earth. During the peak deceleration period, 220 s before the landing, there was a 30-s signal outage as shown in Figure 3-13. This 30-s communication gap was possibly due to blackout. It may also be due to some other effects. This suggests a much higher electron density around the capsule than expected by the model in previous studies (as shown in Figure 3-12). Thus, a more accurate plasma distribution should be recalculated using an updated Martian atmospheric density and composition model.

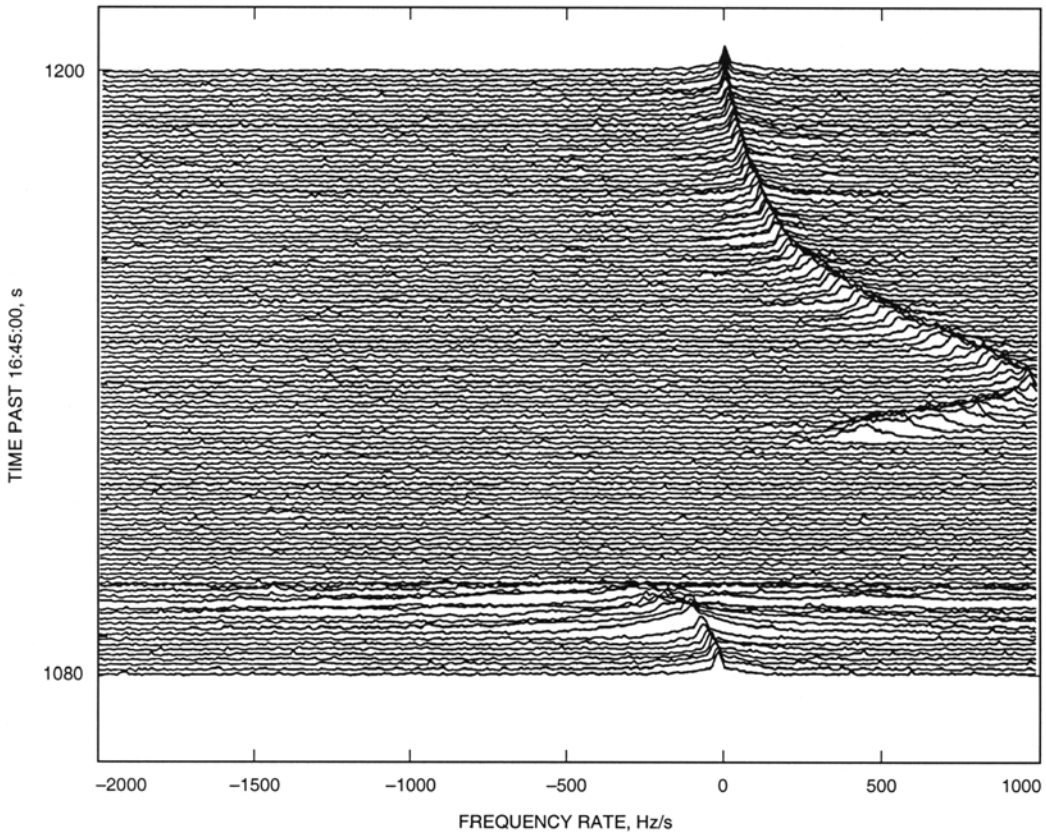

Figure 3-13. Tracking Signals During Mars Pathfinder Atmospheric Entry Phase. The plot shows the Doppler frequency peak ramp rate (i.e., signal derivative) vs. time for the peak deceleration event. There was a 30-s signal outage beginning at 17:03:20 UTC (1100 s past 16:45:00) (from Wood et al., 1997).

Currently, some of the proposed solutions for communication blackout are:

1. Place the antenna where the plasma is diluted (e.g., on the lee side) and communicate by a relay orbiter.
2. Inject some electron-absorbing liquid chemicals into the flowfield to neutralize the plasma [Cuddihy et al., 1963].
3. Increase the frequency of transmission signals from X-band into Ka-band [Brummer, 1963].
4. Apply a magnetic field to the plasma and allow the whistler-mode wave to propagate through a gyrofrequency window [Leblanc and Fujiware, 1996].

For near future Martian atmospheric entry and manned landing programs, the first three methods are more feasible solutions for overcome the communication blackout effects, but finding the best solution remains to be experimentally tested.

3.6 Summary and Recommendations

Compared to Earth's troposphere, the Martian troposphere has a relatively small effect on radio wave propagation. The refractive index of the Martian troposphere is about two orders of magnitude smaller than that of Earth's. Attenuation due to clouds and fog depends largely on their water contents. So far we have little knowledge because direct cloud measurements are not yet available. However, Martian clouds are expected to have relatively less water liquid content because the clouds have a small optical depth. At most, the clouds are expected to be similar to terrestrial high-level cirrus clouds. Martian fog and aerosols (haze) have also been found to have little optical depth.

Even though the Martian tropospheric radio refractivity has a small value, it can still cause ray bending and multipath effects. We recommend that researchers perform an accurate calculation on the excess phase and group delays (range and time delays). Other effects (such as range rate errors, appearance angle deviation, defocusing loss on Mars, etc.) also need to be estimated. Ice depolarization effects on radio waves are still unknown, although they are expected to be small because of the lower optical depth and thinner cloud layer.

Although not as pronounced as on Earth, clouds are a common feature on Mars. The Martian atmosphere has only a trace of water vapor; however, the temperature and pressure are such that the atmosphere is usually close to saturation and produces clouds. Even from Earth-based telescopes, clouds have been observed by transient brightening on the surface of Mars. Numerous cloud patterns have been seen from the Mariner and Viking spacecraft and have been classified into various categories [Carr, 1981; French et al. 1981]. The optical depths of Martian clouds and fogs are about 1.0. Thus, it is expected that they have little attenuation on microwave propagation and optical communications.

The optical depth of Martian aerosol dust is about 0.5. Its attenuation effect on radio wave propagation is smaller than that of the Martian clouds. However, the amount of Martian aerosols should be monitored, and the maximum height to which aerosols extend in the atmosphere should be determined. Also, the size and shape of the aerosol particles should be measured.

In general, the Martian atmospheric environment is quite good for optical communications because of its thinner atmosphere, except during dust storms because the optical depth of Martian clouds is only one fifth of Earth clouds. Martian aerosols can cause some attenuation to laser beams; however, this effect is very small compared with that of aerosols at Earth.

During spacecraft atmospheric entry, signal transmissions will be significantly degraded (blackout). Even though a great effort has been made in the past 30 years, this problem has never been completely solved. A 30-s communication disruption at X-band during the Mars Pathfinder descent was probably caused by plasmasheath blackout. Two basic directions for reduction of the problem are indicated:

(1) Increase the signal frequency to a point where its value is higher than the plasma frequency value.

(2) Reduce the plasma electron density by modifying the plasma.

References

Annis, J., The atmosphere of Mars and optical communications, *TDA Progress Report 42-91*, Jet Propulsion Laboratory, Pasadena, CA, 124, November 15, 1987.

Battan, L.J., *Radar Observation of the Atmosphere*, U. of Chicago Press, 1973.

Bean, B.R. and E.J. Dutton*., Radio Meteorology*, Dover Publications Inc., New York, USA, 1966.

Boukhobza, M., Communication blackout during earth-atmosphere entry of capsules*, NASA Technical Report*, 97N25663, May, 1997.

Briggs, G., et al., Martian dynamical phenomena during June–November 1976: Viking orbiter results, *J. Geophys. Res., 82*, 4121, 1977.

Brummer, E.A., X-band telemetry systems for reentry research, *NASA Technical Report* 63N14953, April, 1963.

Carr, M.H., *The surface of Mars*, Yale University Press, 1981.

Chadwick, K.M., Plasma and aerothermal measurements on a hypervelocity re-entry vehicle, *J. Spacecraft Rockets, Vol. 34*, 602-608, 1997.

Christensen, P.R. and R.W. Zurek, Martian north polar hazes and surface ice: Results from the Viking survey/composition mission, *J. Geophys. Res., 89*, 4587, 1984.

Cuddihy, W.F., et al., A solution to the problem of communications blackout of hypersonic reentry vehicles, *NASA Technical Report*, 71N70235, Oct. 1963.

Dunn, M.G., Comparison between predicted and measured blackout boundaries for earth of Apollo, *NASA Technical Reports*, 71N21104, Jan. 1970.

French, R.G., et al., Global patterns in cloud forms on Mars, *Icarus, 45*, 468, 1981.

Golombek, M.P., et al., Overview of the Mars Pathfinder mission and assessment of landing site predictions, *Science, 278,* 1743, 1997.

Grose, W.L., et al., An analysis of communications blackout for Pioneer Venus entry probes, *AIAA Paper 75-182*, Jan. 1975.

Gunn, K.L.S., and T.W.R. East, The microwave properties of precipitation particles, *Quart. J. Roy. Meteor. Soc., vol. 80*, 522, 1954.

Hinson, D.P., F.M. Flasar, R.A. Simpson, J.D. Twicken, and G.L. Tyler, Initial Results from Radio Occultation Measurements with Mars Global Surveyor, *J. Geophy. Res.-Planet, 104,* 26297, 1999.

Horton, T.E., The JPL thermochemistry and normal shock computer program, Jet Propulsion Laboratory, Pasadena, CA*, Technical Report No. 32-660*, Nov. 1, 1964.

Huber, P.W., Research approach to reentry communications blackout, Presented in the Conference on Langley research related to Apollo Missions, *NASA SP-101*, June, 22, 1965.

Kahn, R., The spatial and seasonal distribution of Martian clouds and some meteorological implications, *J. Geophys. Res., 89,* 6671, 1984.

Keating, G.M., et al., The structure of the upper atmosphere of Mars: In situ accelerometer measurements from Mars Global Surveyor, *Science*, 279, 1672, 1998.

Landis, G., Dust obscuration of solar arrays, *Acta Astronautica, Vol. 38*, No. 11, 895-891, 1996.

Leblanc, J.E., and T. Fujiware, Comprehensive analysis of communication with a reentry vehicle during blackout phase, *Trans. Japan Soc. Aero. Space Sci*., *Vol. 39*, 211-221, Aug. 1996.

Leovy, C., Martian meteorological variability, The Mars reference atmosphere, Ed. by Kliore, A.J*., Adv. Space Res., 2*, 2, 1982.

Lin, Shao-Chi and J.D. Teare, Rate of ionization behind shock waves in air. II. Theoretical interpretations, *Phys. Fluids, Vol. 6*, 355-375, Mar. 1963.

Ludlam, F.H., *Clouds and Storms*, Pennsylvania State U. Press, 1980.

Mitchell, F.H., Jr., Communication-system blackout during reentry of large vehicles, *Proceedings of the IEEE, Vol. 55*, 619-626, 1967.

Nordgard, J.D., A Martian entry propagation study, *Radio Sci., Vol., 11*, 947-957, 1976.

Olte, A., Study of plasma sheath associated with communications blackout: Final report, *NASA Technical Report 67N19139*, Dec. 1966.

Pollack, J.B. et al., Properties of aerosols in the Martian atmosphere, as inferred from Viking Lander imaging data, *J. Geophys. Res., 82*, 4479, 1977.

Pollack, J.B. et al., Properties and effects of dust particles suspended in the Martian atmosphere, *J. Geophys. Res., 84,* 2929, 1979.

Rieder, R. et al., The chemical composition of Martian soil and rocks returned by the mobile alpha proton X-ray spectrometer: Preliminary results from the X-ray mode, *Science, 278,* 1771, 1997.

Schofield, J.T. et al., The Mars Pathfinder atmospheric structure investigation/meteorology (ASI/MET) experiment, *Science, 278,* 1752, 1997.

Seiff, A., Post-Viking models for the structure of the summer atmosphere of Mars, The Mars reference atmosphere, Ed. by Kliore, A.J., *Adv. Space Res., 2*, 2, 1982.

Slobin, S.D., Microwave noise temperature and attenuation of clouds: Statistics of these effects at various sites in the United States, Alaska, and Hawaii, *Radio Sci.,* 17, 1443, 1982.

Spencer, D.F., An evaluation of the communication blackout problem for a blunt Mars-entry capsule and a potential method for the elimination of blackout, Jet Propulsion Laboratory, Pasadena, CA, *Technical Report No. 32-594*, April 15, 1964.

Team, R., Characterization of the Martian surface deposits by the Mars Pathfinder rover, Sojourner, *Science, 278,* 1765, 1997.

Thorpe, T., Viking Orbiter observations of atmospheric opacity during July–November 1976, *J. Geophys. Res., 82*, 4151, 1977.

Tillman, J.E. et al., Frontal systems during passage of the Martian north polar hood over the Viking Lander 2 site prior to the first 1977 dust storm, *J. Geophys. Res., 84*, 2947, 1979.

Tischer, F.J., A rough estimate of the "blackout" time in re-entry communications*, NASA Technical Report 64N29516*, GSFC, June, 1962.

Tischer, F.J., Communication blackout at re-entry, *NASA Technical Report 64N13335*, Sept. 1963.

Vasilleva, L.I., et al., Determination of the duration and limits of communication loss upon entry of the descent vehicle of the space probe Mars 6 into the Martian atmosphere, *Kosmich. Issled., 14,* 610, 1976.

Wood, G.E., et al., Mars Pathfinder entry, descent, and landing communications, *TDA Progress Report 42-131*, Jet Propulsion Laboratory, Pasadena, CA, 1–19, November 15, 1997.